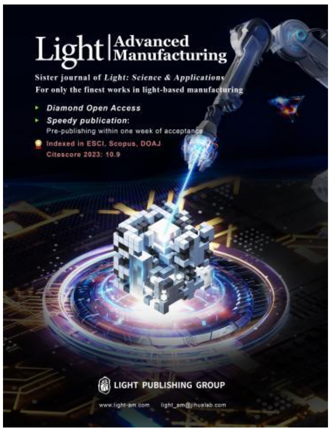

Annealing-Driven Absorption Mechanisms in TiO2-Ta2O5 High-Reflection Coatings

Ruichen Song, Kongxu Zhu, Yuheng Jiang, Ying'ao Xiao, Yuxiang Wang, Zhilin Xia and Xusheng Xia

Cite this article as: Ruichen Song, Kongxu Zhu, Yuheng Jiang, Ying'ao Xiao, Yuxiang Wang, Zhilin Xia and Xusheng Xia. Annealing-Driven Absorption Mechanisms in TiO2-Ta2O5 High-Reflection Coatings. *Light: Advanced Manufacturing* accepted article preview 6 June 2026; doi: 10.37188/lam.2025.094

Received 11 November 2025; revised 5 June 2026; accepted 5 June 2026;
Accepted article preview online 6 June 2026

Annealing-Driven Absorption Mechanisms in TiO_2-Ta_2O_5 High-Reflection Coatings

Ruichen Song[1,2], Kongxu Zhu[2], Yuheng Jiang[2], Ying'ao Xiao[2], Yuxiang Wang[2], Zhilin Xia[1,2,*], and Xusheng Xia[1,3,*]

[1] State Key Laboratory of Advanced Glass Materials, Wuhan University of Technology, Wuhan 430070, China

[2] School of Materials Science and Engineering, Wuhan University of Technology, Wuhan 430070, China

[3] School of Physics and Mechanics, Wuhan University of Technology, Wuhan 430070, China

Corresponding author: xiazhilin@whut.edu.cn (Z. X.); xsxia@whut.edu.cn (X. X.)

Abstract

Optical absorption is a performance-limiting factor in high-power laser components. This paper reports the deposition of a series of TiO_2-Ta_2O_5 high-reflection (HR) coatings for 1064 nm wavelength using electron beam ion-assisted deposition (EB-IAD), followed by thermal annealing at temperatures ranging from 473 to 873 K. The experimental results indicated that the annealing temperature significantly influenced the absorption characteristics of the TiO_2-Ta_2O_5 coatings. Unlike the conventional view that absorption is primarily governed by stoichiometry, this study reveals that although the oxygen vacancy concentration decreases with increasing annealing temperature, typically leading to reduced absorption, the absorption of the coating actually increases beyond a certain annealing temperature threshold. This indicates that factors other than the oxygen vacancies also influence the absorption properties of the film. By combining experimental characterisation, molecular dynamics simulations, and ab initio calculations, we propose that the increase in absorption at higher annealing temperatures is closely connected to structural changes in the coating, particularly localised crystallisation and phase separation within the amorphous TiO_2-Ta_2O_5 film. At the optimal annealing temperature, an HR mirror fabricated using the EB-IAD method exhibited an absorption as low as 1.3 ppm. This work not only deepens the understanding of the absorption mechanisms in composite oxide laser films, but also offers new insights and solutions for the low-cost, large-scale production of high-power laser components.

Keywords: Thermal annealing, TiO_2-Ta_2O_5 films, Low absorption mirrors

Introduction

High-power laser components play a crucial role in key applications such as industrial precision processing, free-space quantum communication, and inertial confinement fusion[1–3]. The high-reflection (HR) coatings used in these components primarily enhance the laser transmission efficiency and enable precise laser control. Absorption is a critical metric for evaluating the optical performance of HR coatings, particularly in high-power laser applications, as it determines the lifespan and operational stability of the equipment[4].

HR mirrors are typically constructed by stacking high refractive index (H) and low-refractive index (L) materials[5]. SiO_2 is an almost irreplaceable L material owing to its extremely low absorption across the ultraviolet to near-infrared spectrum. Commonly used H materials include metal oxides, such as HfO_2, Ta_2O_5, and Nb_2O_5. Among these, Ta_2O_5 is an excellent HR coating material owing to its relatively high refractive index, broad bandwidth, and favourable cost-effectiveness[6]. Chen et al.[7] deposited Ta_2O_5-based HR films using a dual-source ion-beam sputtering (IBS) system. After annealing at 673 K, these films exhibited low absorption of 1.2 part per million (ppm) at 1064 nm, playing a crucial role in enhancing the performance of high-energy lasers and high-precision optical systems. Current research predominantly attributes mirror absorption to H materials[5]. A promising approach to further reduce the absorption of these materials involves the use of composite films. Elements such as Ti, Zr, W, Co, Hf, and Si can be introduced as dopants into H layers to modulate the structure and absorption properties[8,9]. The Laboratoire des Matériaux Avancés(LMA, Lyon, France) reported IBS-fabricated Ti-doped Ta_2O_5 mirrors exhibiting an absorption of 0.21 ppm, as measured by photothermal deflection, which have been deployed in gravitational wave detectors[10].

Currently, most HR films with extremely low absorption are prepared using IBS[8,10–12]. Films produced by this method exhibit smooth, dense surfaces; however, IBS deposition systems are costly, and only a handful of laboratories can afford large-scale coating systems. Furthermore, the deposition efficiency of IBS is relatively low, resulting in extended processing times for the HR films[13]. In contrast, electron beam ion-assisted deposition (EB-IAD) offers significant advantages for large-scale batch production of laser component coating owing to its relatively low cost and high efficiency[14]. Nevertheless, reports on the use of this method to fabricate ultralow-absorption films remain scarce. Therefore, investigating the absorption mechanism of these films, summarising patterns for reducing their absorption, and integrating these insights with the EB-IAD method holds promise for more efficient production of ultralow-absorption thin films. Furthermore, previous studies have suggested that oxygen vacancies may be the primary cause of absorption in metal oxides, although structural factors may also play a role[15–17]. However, these effects remain unexplored. Specifically, the relationship between the film composition, microstructure, and absorption at different annealing temperatures warrants further investigation.

Therefore, this study investigates the mechanism by which annealing affects the optical absorption of TiO_2-Ta_2O_5 coated HR mirrors, focusing on the relationship between the chemical composition, microstructure, and absorption at different temperatures. Specifically, classical molecular dynamics (MD) simulations and ab initio calculations were employed to describe the structural relaxation states and optical property changes during annealing from a microscopic perspective, thereby validating and explaining the experimental findings.

Methods

Fabrication and Characterisation of HR Mirrors

The TiO_2-Ta_2O_5 HR coatings were deposited on super-polished fused silica substrates (JGS1, China) with a diameter of 25.4 mm and a thickness of 2.5 mm. Prior to deposition, the substrates were ultrasonically cleaned and thoroughly rinsed with deionised water (18.2 MΩ·cm). The films were deposited using an EB-IAD system (OPTORUN, Japan OTFC-1300, Optorun Co., Ltd., Japan). The system can process more than 20 substrates in a single deposition run. In this study, all the substrates were coated during the same deposition run to eliminate batch-to-batch variations and ensure high comparability among the samples. The deposition was performed at the substrate temperature of 523 K and chamber base pressure of 1×10^{-4} Pa under an Ar/O_2 mixed atmosphere, where Ar served as the working gas and O_2 as the reactive gas for complete oxidation. Ionic oxygen generated by a radio frequency ion source was employed for assisted deposition at 1000 V and 1100 mA current.

The film structure comprised substrate/(HL)^17 H/air, where H represents TiO_2-Ta_2O_5 containing mass fraction $C_{TiO_2}^{wt}$ of approximately 10% TiO_2 with quarter wavelength optical thickness (QWOT), and the L is SiO_2 with QWOT. The corresponding designed physical thicknesses of the H and L layers were approximately 127 nm and 183 nm, respectively. In this study, an HR mirror was designed with a high-index QWOT termination layer. It should be noted that, in practical coating designs, two QWOT capping layers are often employed to enhance the stability of the mirror against environmental influences, particularly under high-power laser irradiation. In typical applications, the additional outermost layer is subjected to very high electric field intensities and, depending on the material quality, may contribute to an increase in the overall absorption of the coating system. The present work is not intended to develop a fully electric field-optimised coating design. Instead, a structurally simple and experimentally reproducible coating architecture was adopted to systematically investigate the annealing-induced evolution of the absorption and microstructure, particularly within the H layers.

Ta_2O_5 and Ti_3O_5 granules with particle sizes of 1-3 mm and a purity of 99.99% were used as the source materials for the H layer. Quartz rings (SiO_2, 99.99%) were used as the source material for the L layer. All these evaporation materials were supplied by Zhongchengda Applied Materials Co., Ltd. (APG, China).The specific doping configurations and monitoring procedures were established in a previous study[17]. The coating annealing process was performed in a muffle furnace under air atmosphere, with temperature changes following a programmed control sequence. The target holding temperatures for annealing were set at 473 –873 K, with intervals of 100 K each. The annealing process involved heating from room temperature (~300 K) to the target temperature, holding for 10 h, and then cooling to room temperature. Both heating and cooling rates were maintained at 100 K/h.

Transmittance of all samples was measured using a Lambda 750S UV-Vis-NIR spectrophotometer with an accuracy of ±0.0006 A. Weak absorption of the coatings before and after annealing was characterised using the photothermal lens method. The measurement procedure and uncertainty analysis followed the standard GB/T 44605-2024 and previously reported methodologies[18]. A 1064 nm pump beam with a power of 4 W was used to induce the thermal response, and a 632 nm He–Ne laser served as the probe beam. For each sample, measurements were performed at three locations: one at the centre and two at half of the sample radius. Two repeated measurements were performed at each location. Film composition was characterised using X-ray photoelectron spectroscopy (XPS) with an AlKα excitation source (hv = 1486.6 eV) on a Thermo K-Alpha instrument (Thermo Fisher Scientific, Waltham, MA, USA). The analysis chamber vacuum level was maintained at 5×10^{-9} mbar. Testing employed a passing energy of 50 eV with 0.1 eV increments, utilising the C 1s = 284.80 eV binding energy as the calibration standard for charge correction[19]. The binding energy uncertainty was estimated to be ±0.1 eV, considering the instrumental energy resolution and charge correction. All spectra were processed and fitted using Avantage software (Thermo Fisher Scientific). Grazing-incidence X-ray diffraction (GIXRD) characterisation of the films was performed using an Empyrean XRD instrument (Malvern Panalytical B.V., Almelo, the Netherlands) to observe crystallisation phenomena at an incidence angle of 0.5°. T The surface topography of the films was determined using atomic force microscopy (AFM; NanoWizard Sense+, Bruker Nano GmbH, Berlin, Germany) integrated with a ZEISS LSM 900 confocal laser scanning microscope (Carl Zeiss Microscopy GmbH, Jena, Germany) over a 20 μm × 20 μm scanning area. Each sample was tested at three distinct surface locations to confirm homogeneity. The bonding changes during coating annealing were characterised using Fourier transform infrared (FTIR) and Raman spectroscopy. Single-point reflectance maps of the films were obtained using a Nicolet iS50 iN10 FTIR spectrometer (Thermo Fisher Scientific, Waltham, MA, USA). Raman spectra of the HR mirrors were recorded before and after annealing using a LabRAM Odyssey Raman spectrometer(HORIBA France SAS, Palaiseau, France) equipped with a 532 nm laser.

Development and Computation of Annealing Models for the TiO_2-Ta_2O_5 System

The structural evolution of amorphous Ti-Ta_2O_5 was investigated using classical MD simulations performed using the LAMMPS package developed by Sandia National Laboratories[20]. The interatomic interactions among the Ta, O, and Ti atoms were described using the Morse-BKS (M-BKS) potential developed by Trinastic et al.[21]. The M-BKS potential is based on the original BKS potential, with an additional Morse term introduced to account for the covalent contributions of Ta–O and Ti–O bonds. The total interaction energy can be expressed as follows:

$$\Phi_{ij}^{M-BKS} = \frac{q_i q_j}{r_{ij}} + A_{ij} e^{\left(\frac{-r_{ij}}{\rho_{ij}}\right)} - \frac{C_{ij}}{{r_{ij}}^6} + D_{ij}\left(1 - e^{(-a_{ij}(r_{ij} - r_e))}\right)^2 \qquad (1)$$

where Φ_{ij}^{M-BKS} denotes the total interaction energy between atoms i and j, $\frac{q_i q_j}{r_{ij}}$ represents the Coulomb interaction, q_i and q_j denote partial charge transfer between the atoms, $A_{ij} e^{\left(\frac{-r_{ij}}{\rho_{ij}}\right)}$ denotes the Pauli repulsion energy, $\frac{C_{ij}}{{r_{ij}}^6}$ denotes the attractive van der Waals interaction, and $D_{ij}\left(1 - e^{(-a_{ij}(r_{ij} - r_e))}\right)^2$ represents the covalent bond. For Ti–O bonds, a stronger covalent *Ti-O*$_{strong}$ interaction was selected, as it better describes the sputtered amorphous TiO_2.

In this study, all potential parameters were adopted directly from Ref. [21], without further modification or refitting. The reported parameters include the partial atomic charges and Morse coefficients determined by the authors by fitting the crystalline lattice constants, elastic properties, and amorphous radial distribution functions (RDFs). The transferability of this potential to both crystalline and amorphous oxide systems has been validated in Ref. [21]. Therefore, it provides a physically consistent framework for modelling the annealing-induced structural evolution in the present Ti-Ta_2O_5 system.

Three TiO_2-Ta_2O_5 systems containing 12.5% Ti were employed for MD simulations, with large (7920 atoms), medium (1760 atoms), and small (220 atoms) model sizes. As illustrated in **Fig. 1**, all the models were derived from the expansion of the same amorphous unit cell, following previously reported procedures[17]. Ti atoms were randomly substituted, and the corresponding number of oxygen atoms was removed to maintain chemical stoichiometry. The original cells were expanded into 1×1×2, 2×2×4, and 4×3×6 super-cells.

All the MD simulations were performed using a Nosé–Hoover thermostat with a time step of 1 fs under periodic boundary conditions. The initial amorphous structures were generated using a thermal annealing-quenching procedure. Because the starting configuration already exhibited a certain degree of structural disorder, a target temperature of 1000 K was employed to eliminate residual structural memory and promote network rearrangement. The specific procedure was as follows. The system was first equilibrated at 300 K for 50 ps under the NVT ensemble (canonical ensemble; constant number of particles, volume, and temperature). It was then heated from 300 K to 1000 K under the NPT ensemble (isothermal–isobaric ensemble; constant number of particles, pressure, and temperature) for over 35 ps. Subsequently, equilibration was conducted at 1000 K for more than 50 ps under NVT conditions. The system was then quenched at 300 K using the NPT ensemble for periods exceeding 35 ps. Finally, an additional 50 ps equilibration under the NVE ensemble (microcanonical ensemble; constant number of particles, volume, and energy) was performed to stabilise the energy. The resulting configuration was used as an as-deposited model.

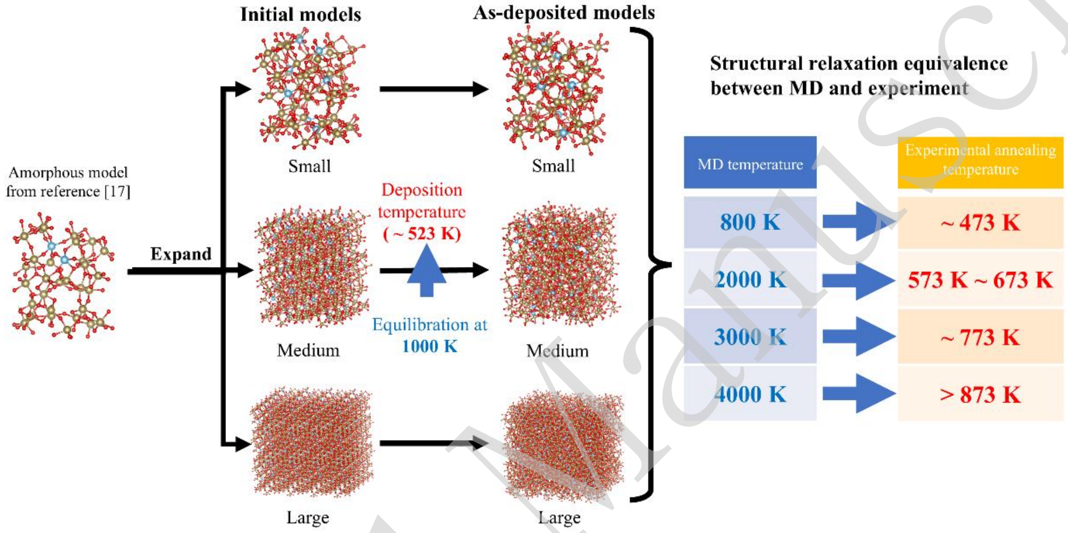

Fig. 1 Construction procedure of the annealed models. All structures were expanded from the same amorphous unit cell following Ref. [17], with random Ti substitution and stoichiometric O adjustment. A 1000 K annealing-quenching procedure was applied to obtain a relaxation state equivalent to the as-deposited structure. The same protocol was used for annealed models, and equivalence was assessed based on structural relaxation rather than absolute temperature.

Annealing simulations were subsequently performed on this structure following the same protocol, with the target temperatures set to 800, 2000, 3000, and 4000 K. Heating and cooling were conducted in 300 K increments at a rate of 20 K/ps. The structures equilibrated at 300 K under the NVE ensemble were selected as the final annealing models. For each target temperature, five independent simulations with different random initial seeds were performed to ensure the statistical reliability.

It should be emphasised that the thermostat temperatures employed in the simulations were not intended to establish a direct one-to-one correspondence with experimental annealing temperatures. In MD simulations, temperature serves as an accelerated sampling parameter that enables structural rearrangements within accessible computational timescales. Because of the intrinsic limitation of MD simulations in the picosecond–nanosecond regime, elevated target temperatures are commonly adopted to overcome kinetic barriers during the construction and relaxation of amorphous structures[22,23]. Therefore, the equivalence between the simulation and experiment was evaluated based on the degree of structural relaxation (e.g. stabilisation of the density and radial distribution functions) rather than the absolute temperature value. This approach has been widely employed in simulations of amorphous oxides and glassy systems[24,25].

The electronic structure and absorption properties of the small models were calculated by density functional theory (DFT) using the Vienna ab initio simulation package (VASP)[26]. The Ta, O, and Ti atoms used projected augmented wave (PAW) pseudopotentials with valence electron configurations of $5p^6 5d^3 6s^2$, $2s^2 2p^4$, and $3s^2 3p^6 4s^1 3d^3$, respectively. Structural relaxation and self-consistent calculations employed the Perdew-Burke-Ernzerhof generalised gradient approximation to describe the exchange-correlation functional[27]. Spin polarisation was included to account for possible defect-induced localised states in the doped or oxygen-deficient configurations. The convergence threshold for electronic structure iterations was set at 10^{-5} eV. Atomic forces converged to within 0.02 eV/Å, with the cutoff energy increased to 520 eV. Because the system comprises 220 atoms, only the Γ point is sampled during structural relaxation. The k-point sampling for self-consistent calculation increased to 2×2×2. The Heyd-Ernzerhof-Scuseria (HSE06) hybrid functional was used to calculate the electronic structure and optical properties, yielding relatively accurate results[28]. Due to its high computational demands, k-point sampling for these calculations also utilises the Γ point.

The linear optical properties of the system can be obtained from the frequency-dependent complex dielectric function $\varepsilon(\omega)$.

$$\varepsilon(\omega) = \varepsilon_1(\omega) + \varepsilon_2(\omega) \tag{2}$$

where $\varepsilon_1(\omega)$ and $\varepsilon_2(\omega)$ represent the real and imaginary parts of the dielectric function, respectively, and ω denotes the photon frequency. The formula for the imaginary part $\varepsilon_2(\omega)$ of the dielectric function is

$$\varepsilon_2(\omega) = \frac{4\pi^2 e^2}{\Omega} \lim_{q\to 0} \frac{1}{q^2} \times \sum 2 w_{\mathbf{k}} \delta(E_c - E_v - \omega) \, |\langle c|\mathbf{e}\cdot\mathbf{q}|v\rangle|^2 \tag{3}$$

where $\langle c|\mathbf{e}\cdot\mathbf{q}|v\rangle$ represents the integral optical transition from the valence state (c) to the conduction state (v), where **e** denotes the polarisation direction of the photon and $\mathbf{q}$ is the electron momentum operator. Integration over $\mathbf{q}$ is performed by summing over $\mathbf{k}$ specific points, each assigned a weighting factor $w_{\mathbf{k}}$. The real part $\varepsilon_1(\omega)$ of the dielectric function can be determined using the Kramers-Kronig relations[29].

$$\varepsilon_1(\omega) = 1 + \frac{2}{\pi} P \int_0^\infty \frac{\varepsilon_2(\omega')\omega'}{\omega'^2 - \omega^2 + i\eta} d\omega' \tag{4}$$

where P denotes the principal value, and η represents the complex shift parameter. The frequency-dependent extinction coefficient $k(\omega)$ can be calculated from the real $\varepsilon_1(\omega)$ and imaginary $\varepsilon_2(\omega)$ parts as follows:

$$k(\omega) = \left(\frac{\sqrt{\varepsilon_1^2+\varepsilon_2^2}-\varepsilon_1}{2}\right)^{\frac{1}{2}} \tag{5}$$

Results and Discussion

Optical Properties Evolution upon Annealing

The spectral responses of the HR mirrors before and after annealing are shown in **Fig. 2**. At approximately 1064 nm, the transmittance of all the samples dropped below 0.1%, rendering the effect of annealing on this wavelength band nearly undetectable. Beyond this wavelength range, the spectra of the films exhibited distinct trends as the annealing temperature increased.

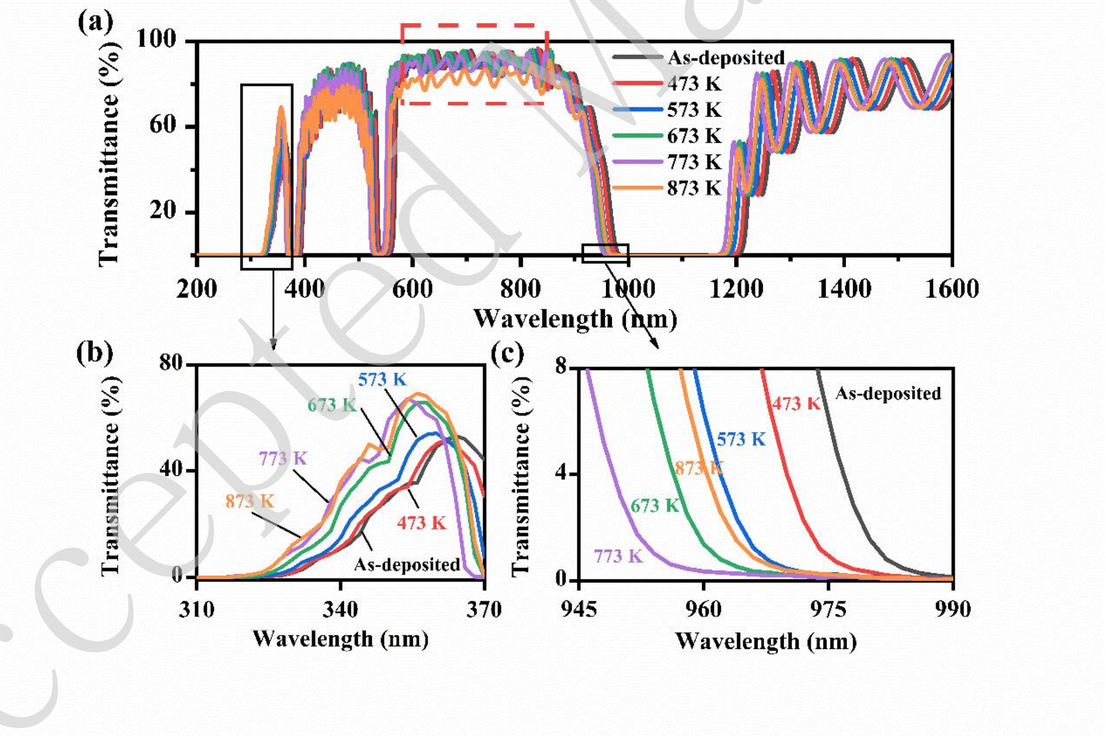

Fig. 2 Transmission spectra of HR mirrors for as-deposited state and after annealing at different temperatures. **a** Transmission spectra in the range of 200–1600 nm. The red dashed box highlights the 600–900 nm band showing significant transmittance changes, where the purple curve (annealed at 773 K) exhibits a relatively minor decrease in transmittance, whereas the orange curve (annealed at 873 K) shows a pronounced decrease. Localised magnification of the transmission spectra in the **b** 310–370 nm and **c** 945–990 nm ranges.

As shown in **Fig. 2a**, the transmittance of the mirror annealed at 773 K decreases near 600–900 nm, a trend that becomes more pronounced at 873 K annealing. AFM results in the next section reveal significant surface roughening on films annealed at ≥773 K. This introduces additional scattering losses, thereby reducing the measured transmittance[30,31]. Therefore, the observed decrease in transmittance in the 600–900 nm range is likely associated with enhanced scattering induced by high-temperature annealing. Nevertheless, direct scattering measurements are required to confirm this contribution quantitatively.

In the ultraviolet region (**Fig. 2b)**, compared to the as-deposited sample, the cutoff edge of the annealed films tended to become steeper, indicating a reduction in the Urbach tail width. The film annealed at 473 K exhibits no significant change in the tail width, which may be attributed to lower annealing temperature than the deposition temperature (523 K). Under lower annealing conditions, the rearrangement of the atomic structures and stress release within the film remain limited. In contrast, films annealed at 573–673 K exhibit a significantly narrower Urbach tail width. At higher annealing temperatures (773–873 K), the trend of Urbach tail reduction weakens, even showing slight rebound. Some studies have suggested that the Urbach tail width reflects the O vacancy defect density and degree of disorder in the internal structure of the film[32]. A lower defect density indicates a more ordered film, resulting in a narrower tail. These results indicated that annealing may reduce the concentration of O vacancies in the film and enhance its structural order.

Additionally, **Fig. 2c** shows that the cutoff position near 980 nm in the sample spectra exhibits a characteristic evolution with the annealing temperature. From the as-deposited state to 773 K, the cutoff position progressively shifts toward shorter wavelengths. Previous studies have attributed this to changes in the effective optical thickness of the film, which is potentially linked to the material relaxation induced by annealing at lower temperatures[33]. At 873 K, the cutoff position ceases to shift further toward shorter wavelengths and instead returns to a position intermediate between the 473 and 573 K annealed samples. This indicated a change in the evolution mechanism of the film material at this temperature. Given that the transition and phase change temperatures of SiO_2 in the L layer are significantly higher than those of TiO_2-Ta_2O_5 in the H layer, combined with the previously described spectral changes across different bands, it can be inferred that under the 773–873 K heat treatment conditions, an evolution mechanism distinct from that observed during the low-to-medium temperature annealing stages may have emerged in the TiO_2-Ta_2O_5 layer. Related issues are further discussed in subsequent sections.

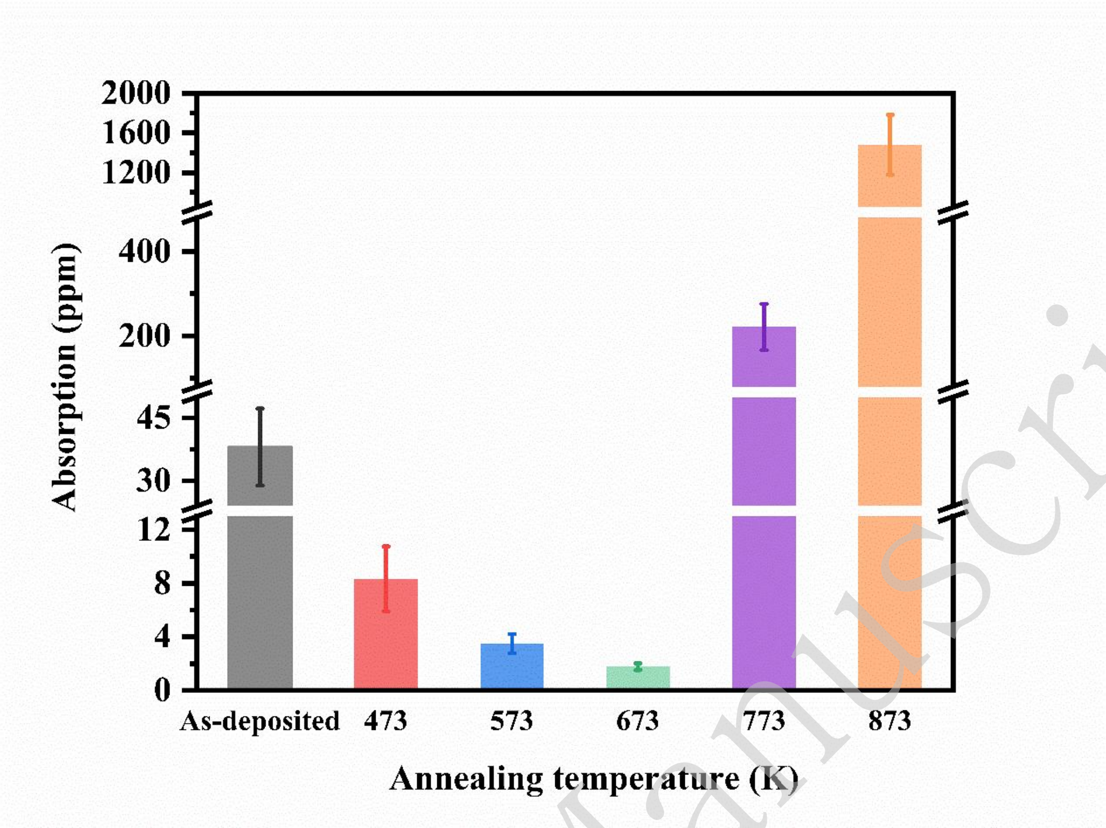

Fig. 3 Surface absorption at 1064 nm for HR mirrors in as-deposited state and after annealing at different temperatures.

The absorption of the thin films was measured at 1064 nm using the photothermal lens method, and the results are shown in **Fig. 3**. The absorption of all films prior to thermal treatment ranged between 30 and 50 ppm. As the annealing temperature increased, the film absorption initially decreased and then increased. As the annealing temperature increased from 473 to 673 K, the film absorption decreased from approximately 5 ppm to 1.3 ppm. Similar trends have been reported in previous studies, indicating that annealing reduces film absorption by suppressing the O vacancies[7,17]. However, for annealing temperatures above 673 K, the film absorption sharply increased to several hundred ppm, exceeding 1000 ppm at 873 K. Reports on such non-monotonic temperature-dependent changes in film absorption are relatively scarce. Lin et al.[34] also reported non-monotonic changes in film absorption with temperature during annealing of HfO_2 films. The mechanism underlying this abrupt shift in absorption after the high-temperature annealing warrants further investigation.

Annealing-Induced Structure and Morphological Evolution

Subsequently, the as-deposited and annealed samples were structurally characterised. GIXRD was employed to collect structural information of the H layer surface. As shown in **Fig. 4**, both the as-deposited films and those annealed at all temperatures exhibit an amorphous state. This indicates that no significant annealing-induced crystallization occurred within the HR mirrors.

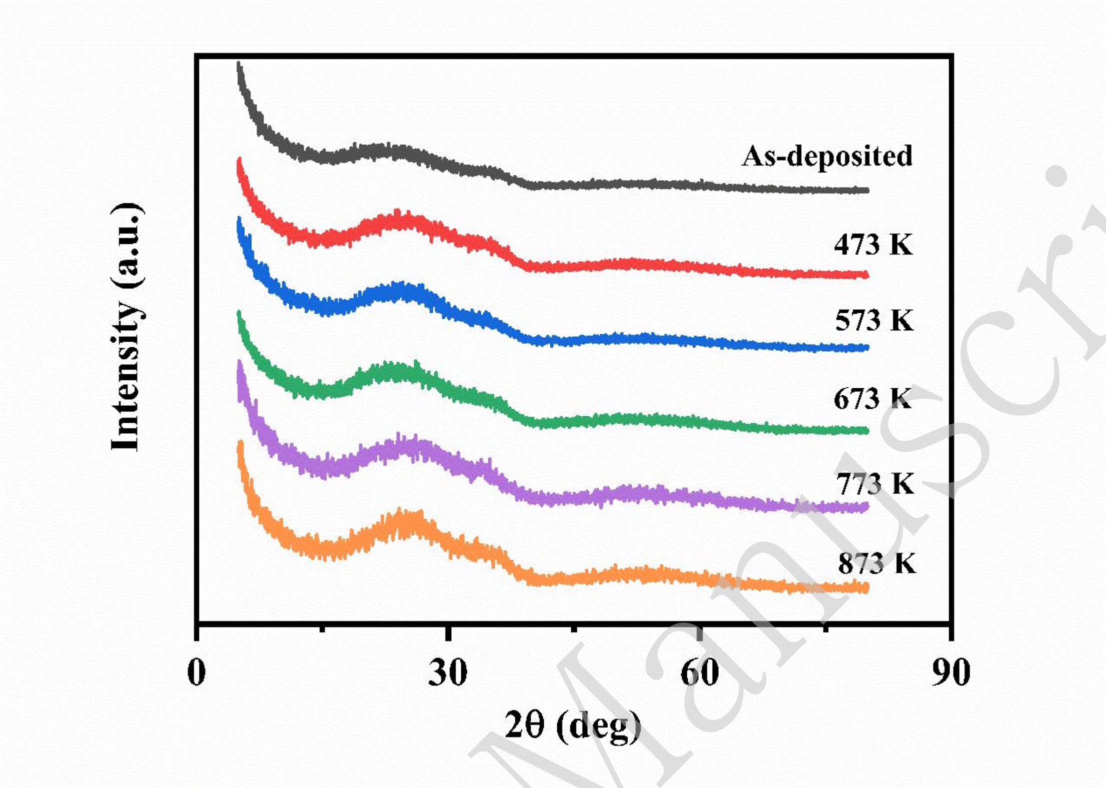

Fig. 4 GIXRD patterns of HR mirrors in as-deposited and annealed states.

AFM was used to characterise the evolution of film surface roughness. The surface topography of the as-deposited state and samples treated at ≤673 K was nearly identical, with no significant grain formation observed (**Fig. 5a–d**). The root-mean-square (RMS) roughness values determined from the topography images further indicate that films annealed at 573 and 673 K exhibit relatively lower RMS roughness (0.730 and 0.562 nm, respectively). This suggests that annealing at moderate-to-low temperatures does not compromise the surface flatness of the film and may even slightly improve the surface morphology.

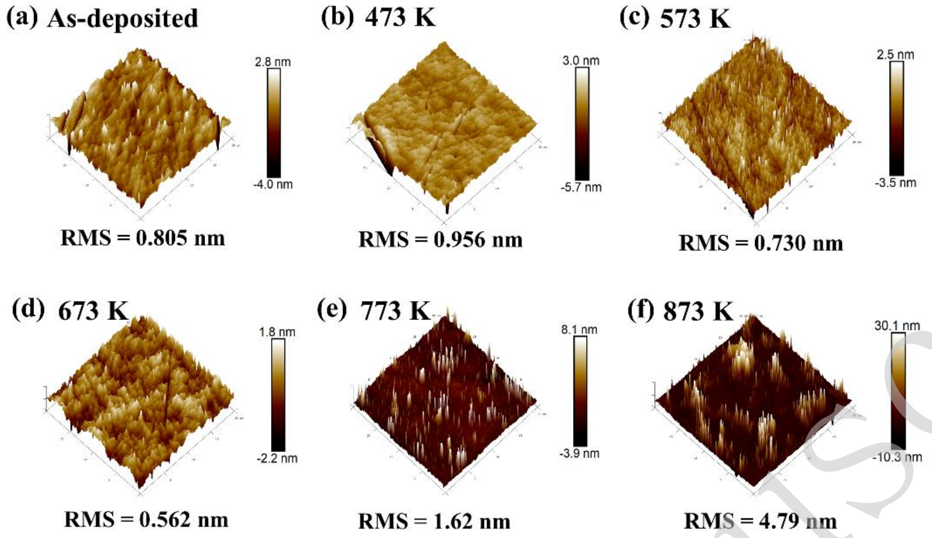

Fig. 5 Surface morphology and RMS roughness of the HR mirrors: **a** as-deposited and annealed at **b** 473, **c** 573, **d** 673, **e** 773, and **f** 873 K. The RMS roughness was determined by AFM.

However, the RMS values increased to 1.62 and 4.79 nm for the annealing temperatures of 773 and 873 K, respectively. Compared with **Fig. 5a–d**, Fig. 4e shows a small number of isolated spike-like protrusions. Considering the crystallisation temperature difference between Ta_2O_5 (~973 K) and TiO_2 (~673 K), this phenomenon may be related to local ordering or initial crystallisation of the TiO_2 component[9,17]. Further analysis of the sample annealed at 873 K (**Fig. 5f**) reveals an increased number of protrusions, along with some degree of aggregation and size enlargement. However, these protrusions remained spatially dispersed and failed to form continuous macroscopic crystalline domains. Their morphologies differ distinctly from the regular grain structures typically observed in polycrystalline films[4,35]. This indicates that even if locally ordered regions exist, their sizes and volume fractions remain limited. Under these conditions, the crystal domain size may fall below the critical threshold required for XRD detection, and the overall crystalline volume fraction may be insufficient to generate resolvable diffraction peaks. Therefore, the absence of distinct diffraction peaks in the GIXRD patterns (Fig. 4) is understandable.

Chemical-State Evolution and Electronic Environment

The films were characterised in their as-deposited state and after annealing at 573 and 873 K to determine their composition. Based on XPS, the primary target was H-layer TiO_2-Ta_2O_5[19]. **Fig. 6a–c** display the XPS spectra of O in the tested samples. O_I corresponds to lattice O, whereas O_{II} and O_{III} typically involve hydroxyl and surface-adsorbed O[36]. The deconvolution results show that the relative contributions of the O_{II} and O_{III} components decreased after annealing, suggesting that annealing reduced hydroxyl- and surface-adsorption-related species on the film surface.

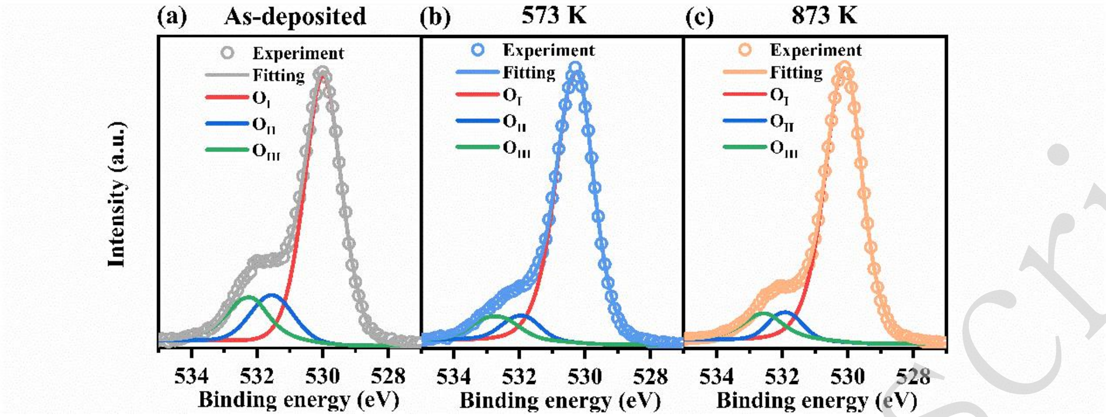

Fig. 6 Surface chemical observation of HR mirrors. XPS patterns of O: **a** as-deposited sample; sample annealed at **b** 573 and **c** 873 K. O_I corresponds to lattice oxygen, O_{II} and O_{III} typically involve hydroxyl and surface-adsorbed oxygen.

The atomic percentages of Ta, Ti, and O in **Table 1** were obtained from the XPS analysis. The reported values were normalised to 100 at.%. Based on the above element content, the mass fraction of TiO_2 ($C_{TiO_2}^{wt}$) and the gain and loss of O in the film were calculated.

For the estimation of $C_{TiO_2}^{wt}$, Ti and Ta were treated as forming TiO_2- and Ta_2O_5-equivalent compositions according to their stoichiometric O requirements. Let C_{Ti}, C_{Ta}, and C_O denote Ti (at.%), Ta (at.%), and O (at.%) in Table 1, respectively.

The molar amounts of TiO_2 and Ta_2O_5 are expressed as:

$$n_{TiO_2} = C_{Ti} \tag{6}$$

$$n_{Ta_2O_5} = \frac{C_{Ta}}{2} \tag{7}$$

The corresponding masses are:

$$m_{TiO_2} = n_{TiO_2} \times M_{TiO_2} \tag{8}$$

$$m_{Ta_2O_5} = n_{Ta_2O_5} \times M_{Ta_2O_5} \tag{9}$$

where M_{TiO_2} and $M_{Ta_2O_5}$ are the molar masses of TiO_2 and Ta_2O_5, respectively.

Therefore $C_{TiO_2}^{wt}$ is

$$C_{TiO_2}^{wt} = \frac{m_{TiO_2}}{m_{TiO_2} + m_{Ta_2O_5}} \times 100\% \tag{10}$$

The results indicate that the TiO_2 content in the H layer ranges from 8% to 10%. The slight variation in $C_{TiO_2}^{wt}$ among samples may stem from differences in spatial distribution within the coating equipment.

The O stoichiometry was evaluated using the ratio O_m/O_c, where

O_m is the O (at.%) and

$$O_m = C_O \tag{11}$$

O_c is the theoretical O content calculated from the Ti (at.%) and Ta (at.%). Assuming stoichiometric TiO_2 and Ta_2O_5 formation

$$O_c = 2C_{Ti} + \frac{5}{2}C_{Ta} \tag{12}$$

The ratio O_m/O_c was used to assess deviations from ideal stoichiometry. A value close to one indicates a near-stoichiometric composition, whereas values below or above one suggest O deficiency or excess O, respectively. The O_m/O_c ratio of the as-deposited film was 0.86. After annealing at 573 and 873 K, the O_m/O_c ratios increased to 0.95 and 0.96, respectively. This indicates that annealing at lower temperatures can increase the O content of the film. This confirms the hypothesis that annealing effectively eliminates O vacancies. Notably, compared to samples annealed at 573 K, samples annealed at 873 K exhibited further increases in O_m/O_c ratios. However, as shown in **Fig. 3**, the absorption intensity increases, suggesting that the increased film absorption at higher temperatures may be less correlated with O vacancies.

Table 2 presents the XPS results for Ta, O, and Ti. For the film annealed at 573 K, the core levels of Ta $4f_{7/2}$, O 1s, and Ti $2p_{3/2}$ are located at 26.0, 530.2, and 458.5 eV, respectively. These values are close to the reported core levels of 26.0–26.4, 530.5, and 458.6 eV for the corresponding oxidation states[36–38]. The binding energies of the deposited state and the film treated at 873 K shifted toward lower energies relative to their actual positions in their respective standard XPS spectra. For the as-deposited sample, the mirror annealed at 573 K exhibited an increase in O content (higher O_m/O_c), leading to a higher oxidation state of the system. Consequently, the observed increase in the binding energy can be attributed to changes in stoichiometry[9,39]. However, from 573 to 873 K, O_m/O_c for both is similar, and the O content remained almost unchanged. In the absence of significant compositional or valence state evolution, a consistent negative shift across elements is more likely to stem from changes in the surface potential or enhanced final-state relaxation, rather than from stoichiometric changes. This is in line with observations from XPS studies of charge transfer and binding energy shifts due to surface potential changes[40–42]. Similar binding-energy shifts related to differential charging have been reported for nonconductive oxide systems. Rahimi et al.[42] demonstrated that changes in the charge distribution within a bilayer oxide structure can induce systematic shifts in the O 1s binding energy even in the absence of chemical state evolution. These shifts were attributed to variations in the surface potential and charge redistribution across the metal/oxide interface rather than compositional changes. In the present system, because no evident change in composition or oxidation state was detected between 573 and 873 K, the observed cross-element negative shift is therefore more reasonably associated with modifications in surface potential and final-state screening effects induced by structural evolution at elevated temperature.

Table 1. XPS-based elemental ratio on the film surfaces.

	Ta (at.%)	Ti (at.%)	O (at.%)	$C^{wt}_{TiO_2}$	O_m/O_c
As deposited	26.0	6.8	67.2	8.6	0.85
573 K	23.6	7.1	69.4	9.7	0.95
873 K	23.1	7.3	69.6	10.3	0.96

Note: $C^{wt}_{TiO_2}$ = mass fraction of TiO_2; O_m and O_c are O (at.%), and theoretical O content calculated from the Ti (at. %) and Ta (at. %), assuming stoichiometric TiO_2 and Ta_2O_5 formation.

Table 2. XPS Peak positions of Ta, O, and Ti.

Sample	Ta (eV)	O (eV)	Ti (eV)
	Ta $4f_{7/2}$	O 1s	Ti $2p_{3/2}$
As deposited	25.7 ± 0.1	530.0 ± 0.1	458.2 ± 0.1
573 K	26.0 ± 0.1	530.2 ± 0.1	458.5 ± 0.1
873 K	25.8 ± 0.1	530.1 ± 0.1	458.3 ± 0.1
Reference	26.0–26.4[a]	530.5[b]	458.6[c]

References: [a] 36, 37, [b] 37, and [c] 38.

Bonding Configuration and Local Structural Ordering

FTIR spectroscopy can detect and quantify localised changes in the structural symmetry of a material. **Fig. 7** shows the reflectance spectra of the substrate and samples before and after annealing. For comparison, the spectra of the as-deposited and annealed samples are presented in the same figure. In the low-frequency range (<1500 cm^{-1}), four characteristic spectral bands are observed for the fused quartz substrate at approximately 560, 795, 980, and 1170 cm^{-1}. These bands correlate with the vibrational modes of different types of Si–O–Si groups[43]. After deposition, most of these spectral features remained visible. Moreover, their positions and overall shapes showed only weak dependence on the annealing temperature. Given that the vibrational modes in this spectral range are primarily associated with Si–O–Si bonds, the FTIR response below 1500 cm^{-1} is considered to be predominantly governed by the SiO_2 (L) layer, whereas the contributions from the TiO_2-Ta_2O_5 (H) layer are less pronounced in this region.

Specifically, the spectral band at approximately 1170 cm^{-1} in the substrate reflects the asymmetric stretching vibration of Si–O–Si[44]. This peak shifted toward lower frequencies after coating, indicating that deposited SiO_2 exhibits a looser structure than the fused quartz substrate[45]. Furthermore, a slight blue shift occurs in this band with increasing annealing temperature, suggesting that the deposited silica gradually densifies during thermal treatment, making its structure more similar to that of the substrate.

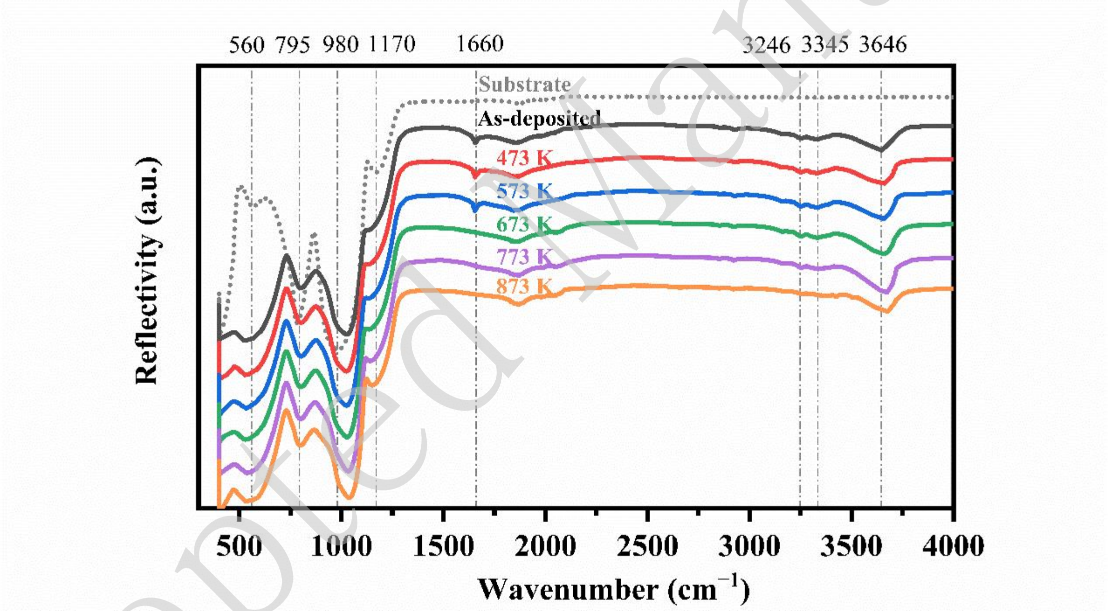

Fig. 7 FTIR spectra of HR mirrors in the as-deposited state and at different annealing temperatures. For comparison, the spectra of the deposited and annealed states are shown in the same figure.

In the high-frequency range (>1500 cm^{-1}), FTIR primarily reveals responses from various water and hydroxyl groups within the film. The substrate spectrum shows no discernible features at the characteristic positions of these bands, suggesting that its contribution to the observed water- and hydroxyl-related signals is limited. The spectral bands at approximately 3650, 3300, and 1660 cm^{-1} in the film samples were primarily correlated with surface hydroxyl groups and various water-bound states[46,47]. In the annealed samples, the spectral band near 1660 cm^{-1}, assigned to the H–O–H bending vibration of adsorbed water, becomes barely discernible for annealing temperatures of 673 K and above. This suggests that adsorbed water molecules on the film surface are substantially reduced after high-temperature annealing. At an annealing temperature of 873 K, the spectral band near 3200 cm^{-1} attributed to water complexes bound to the film surface largely disappears. This form of binding is more difficult to remove than adsorbed water; thus, a higher temperature is required to eliminate the bond. The broad band for 873 K annealed sample, located at 3650 cm^{-1}, is attributed to the O–H stretching vibration of surface hydroxyl groups. This vibration frequency correlated with the surface structure of the film, shifting toward higher frequencies with increasing annealing temperature. This indicated that the surface reconstruction process was accompanied by enhanced hydroxyl bonding. The FTIR spectral results demonstrated that annealing significantly influenced the bonding states of the water and hydroxyl groups within the film. However, the spectral differences between 673 and 773 K annealed samples are relatively minor, suggesting that water content is also unlikely to be the primary factor causing increased film absorption.

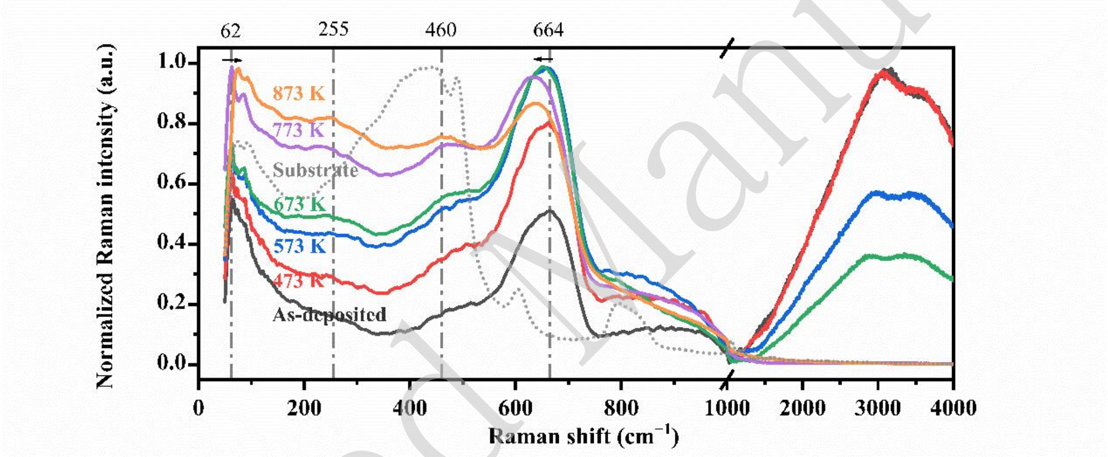

Fig. 8 Raman spectra of HR mirrors in the as-deposited state and at different annealing temperatures. The spectra were normalized to the maximum intensity over the full spectral range. The axis break is used only to improve visual clarity.

Raman spectroscopy can capture the vibrational modes of the chemical bonds in materials, reflecting changes in their microstructures. **Fig. 8** shows the Raman spectra of the substrate along with the deposited coatings at different annealing temperatures. The spectra were normalized to the maximum intensity over the full spectral range. The axis break is used only to improve visual clarity. The fused quartz substrate exhibits characteristic Raman bands at 440, 490, 605, and 800 cm^{-1} within the 50–1300 cm^{-1} range, demonstrating typical amorphous SiO_2 features[48]. In contrast, most of these features were not observed in any of the mirror samples, indicating that the TiO_2-Ta_2O_5 layer exhibited a higher Raman activity, effectively masking the Raman signals from the SiO_2 in the substrate and the L layer.

The left-hand region of **Fig. 8** shows that the Raman response of the coating exhibits distinct variations across the 50–1000 cm^{-1} range at different annealing temperatures.

With increasing treatment temperature, the overall spectrum transitioned from a broadened to a sharpened profile.

The modes at approximately 255 and 460 cm^{-1} primarily originate from the vibrations of the O–Ta–O and O–Ti–O bonds and their coupled interactions[49]. These two vibrational modes gradually emerge and become more pronounced for annealing temperatures exceeding 573 K. Because the spectra were normalized over the full spectral range, the enhanced normalized intensity indicates an increased relative Raman contribution from these local bonding units. This suggests that the local Ta–O and Ti–O bonding environments become more distinct and that the short-range order in the H layer is improved with increasing annealing temperature. The spectral band at approximately 660 cm^{-1} primarily corresponds to symmetric Ta–O vibrations within the TaO_6 octahedra[50]. Its shift toward lower Raman shifts with increasing annealing temperature may indicate a decrease in vibrational frequency, corresponding to an increase in the average Ta–O bond length.[51].

The band features <100 cm^{-1} are mainly associated with vibrational interactions between different polyhedral units within the structural network[52]. With increasing annealing temperature, the normalized intensity of this band increases, indicating an enhanced relative Raman contribution from inter-polyhedral vibrational modes. This suggests that the relative arrangement of polyhedral structural units becomes more stabilized and structurally defined, reflecting improved short- to intermediate-range ordering in the amorphous network. Notably, at 873 K, the band near 62 cm^{-1} shifts toward higher wavenumbers. Dobal et al.[53] reported a similar blue shift of this band with increasing annealing temperature for TiO_2-Ta_2O_5 ceramics, whereas no such shift was observed in annealed pure Ta_2O_5 ceramics. This comparison suggests that the 62 cm^{-1} mode likely reflects interactions between Ti–O and Ta–O polyhedra rather than vibrations among identical Ta–O polyhedra. The observed blue shift indicates a more compact arrangement between the TiO_6 octahedra and Ta–O clusters, corresponding to a reduced average Ti–Ta distance.

In the amorphous TiO_2-Ta_2O_5 network, the Ti and Ta atoms are predominantly interconnected through bridging O atoms. Therefore, the shortening of the average Ti–Ta distance together with the previously discussed increase in the average Ta–O bond length may collectively result in a reduction in the Ti–O bond length. These results suggest that with increasing annealing temperature, the Ti–O polyhedra may undergo contraction, whereas the Ta–O polyhedra evolve in the opposite direction, gradually developing preferential orientations. Such differential evolution may indicate the onset of partial phase segregation and enhanced structural distortion within the amorphous matrix.

Overall, these observations indicate that thermal treatment enhances the medium- and short-range structural orders of the films. The structure evolved from a highly disordered network toward microstructural ordering. This structural evolution was consistent with the trends observed in the AFM results.

The right-hand region of **Fig. 8** displays the Raman spectrum in the 1000–4000 cm^{-1} range. The spectrum of the as-deposited sample exhibited a broad peak centred near 3200 cm^{-1} and extending over a wide spectral range, indicating a strong fluorescence effect. According to previous studies, this fluorescence may have originated from impurity states within the amorphous structure[54,55]. As the annealing temperature increases, the normalized intensity of this fluorescence peak diminishes to varying degrees and essentially disappears at 773 K. Based on the previous test results, we speculated that the change in Raman fluorescence intensity may be related to alterations in the bonding form of Ti within the film. Considering the patterns observed in the lower Raman shift spectrum, the disappearance of the fluorescence may have resulted from the crystallisation transition and phase separation of the Ti–O groups.

For the as-deposited and low-temperature annealed films, two spectral bands remained in the fluorescence background, located at approximately 3100 and 3700 cm^{-1}, reflecting crystalline water and surface-adsorbed water in the film, respectively[56]. As the annealing temperature increases, the normalized intensities of both bands gradually decrease, accompanied by a reduction in the Raman shift. This indicates a decrease in the water content within the film and the associated changes in the bond lengths of the relevant groups. At an annealing temperature of 773 K, both spectral bands disappear along with the fluorescence background.

The experimental results indicate that oxygen vacancies may be responsible for the absorption observed in the films annealed at lower temperatures. For films annealed at higher temperatures, the absorption likely originated from localised crystallisation and phase separation within the amorphous structure. The subsequent sections employ MD and DFT methods to further validate the evolution process and absorption mechanism.

Atomic-Scale Structural Evolution: Molecular Dynamics

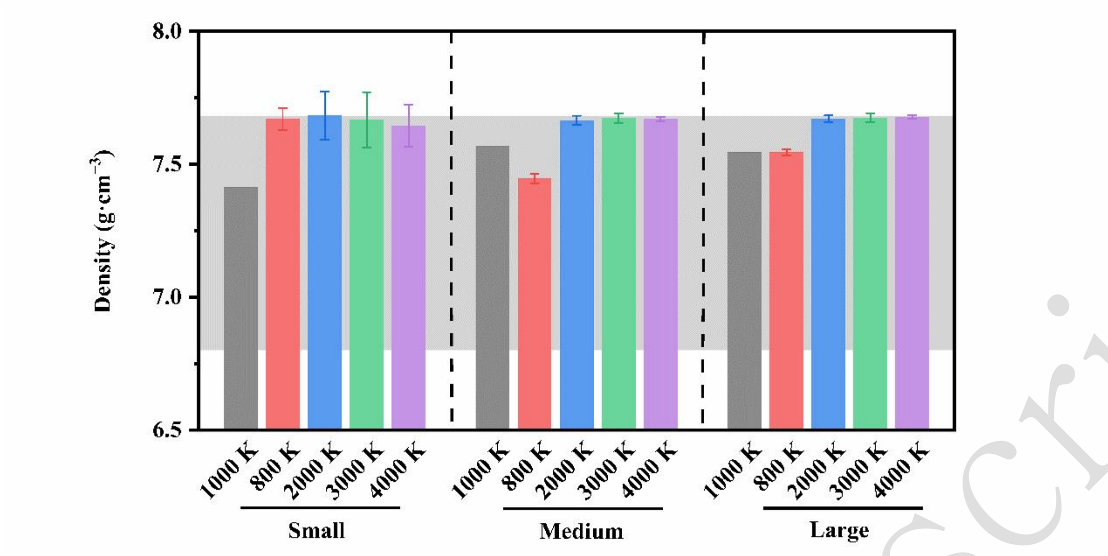

Fig. 9 Statistical summary of the densities of the MD models. The grey shaded region indicates the experimentally reported density range of TiO_2-Ta_2O_5 (6.80–7.68 g·cm^{-3})[24,57]. The 1000 K model, which represents the as-deposited structure, was calculated only once. The annealed models were independently generated using five different random initial seeds, and the averaged densities were plotted; the error bars represent statistical variation among these runs.

To verify the reliability of the constructed models, the densities of all the configurations are summarised in **Fig. 9**. The 1000 K model, which represents the as-deposited structure, was constructed and calculated only once; therefore, no error bars are provided for this case. By contrast, the annealed models were generated using five random initial seeds, and the reported densities correspond to the average values. The error bars indicate statistical fluctuations among these independent runs. The grey shaded region denotes the experimentally reported density range of TiO_2-Ta_2O_5 (6.80–7.68 g·cm^{-3})[24,57].

It can be observed that most simulated densities fall within the experimental range, demonstrating the structural reliability of the constructed models. The relatively large fluctuations observed in the small models can be attributed to finite-size effects. Under NPT conditions, the relative magnitude of the volume fluctuations scales inversely with system size. Smaller systems containing fewer atoms and smaller volumes exhibited more pronounced volume fluctuations, leading to larger statistical variations in density. As the model size increased, these fluctuations were effectively averaged and the density values became more stable.

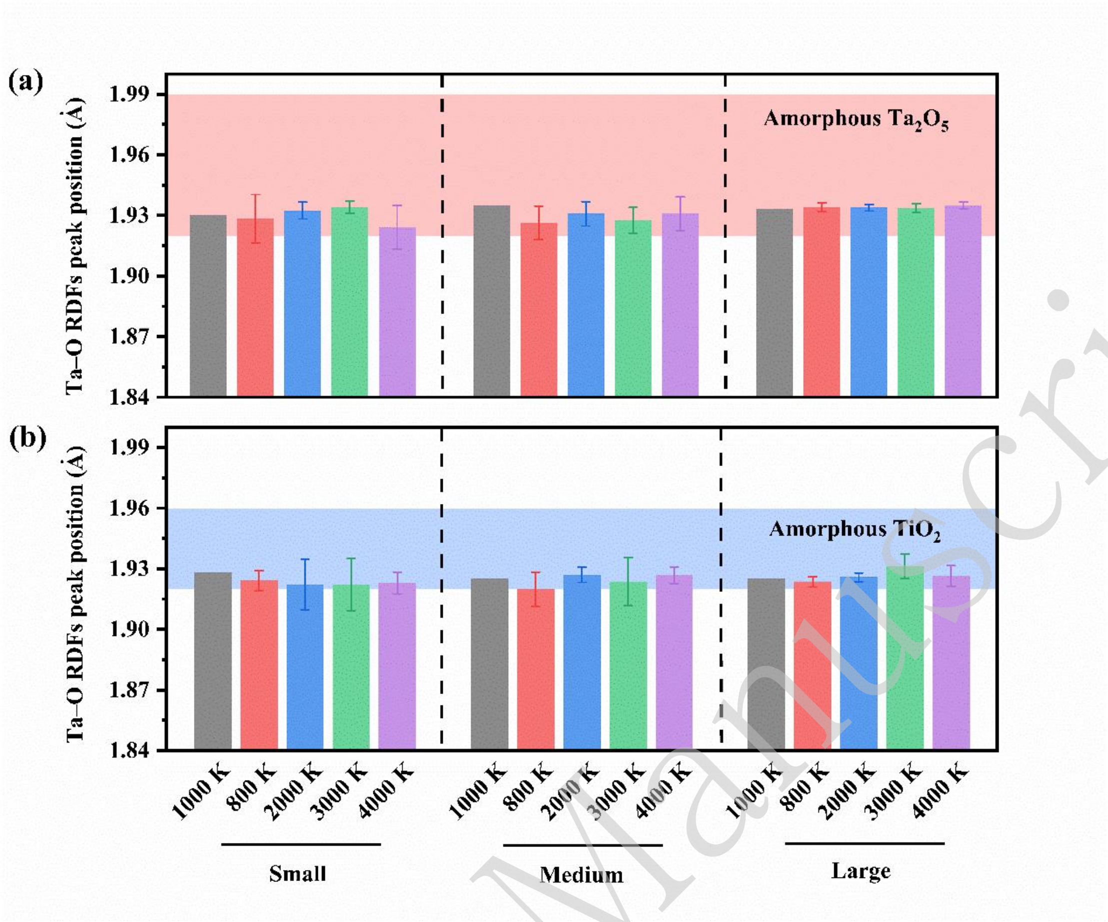

Fig. 10 Radial distribution function (RDF) analysis of all models. Annealed models were independently generated using five random initial seeds; the averaged peak positions with corresponding statistical variations are presented. **a** First-shell peak positions of the Ta–O RDF. The light red shaded region marks the reported bond-length range for amorphous Ta_2O_5 (1.92–1.99 Å)[24,57]. **b** First-shell peak positions of the Ti–O RDF. The light blue shaded region marks the reported bond-length range for amorphous TiO_2 (1.92–1.96 Å)[21,58].

To further examine the local structural characteristics, the RDFs of all models were calculated. The RDF data presented in this study correspond to the time-averaged results over the last 25 ps of the equilibrated NVE trajectories, thereby minimising the influence of instantaneous thermal fluctuations.

Fig. 10 summarises the positions of the first coordination shell peaks for the Ta–O and Ti–O pairs in all models. Consistent with the density analysis, annealed models were independently generated using five random seeds, and the reported values represent the average peak positions with corresponding statistical variations.

As shown in **Fig. 10a**, the Ta–O bond lengths are mainly distributed within 1.92–1.94 Å, which lies within the experimentally reported range for amorphous Ta_2O_5 (1.92–1.99 Å)[24,57]. As shown in **Fig. 10b**, the Ti–O bond lengths are primarily located between 1.92–1.93 Å, also within the reported experimental range for amorphous TiO_2 (1.92–1.96 Å)[21,58], and are overall slightly shorter than the Ta–O bonds. These results indicated that the simulated models reproduced the expected local bonding environments.

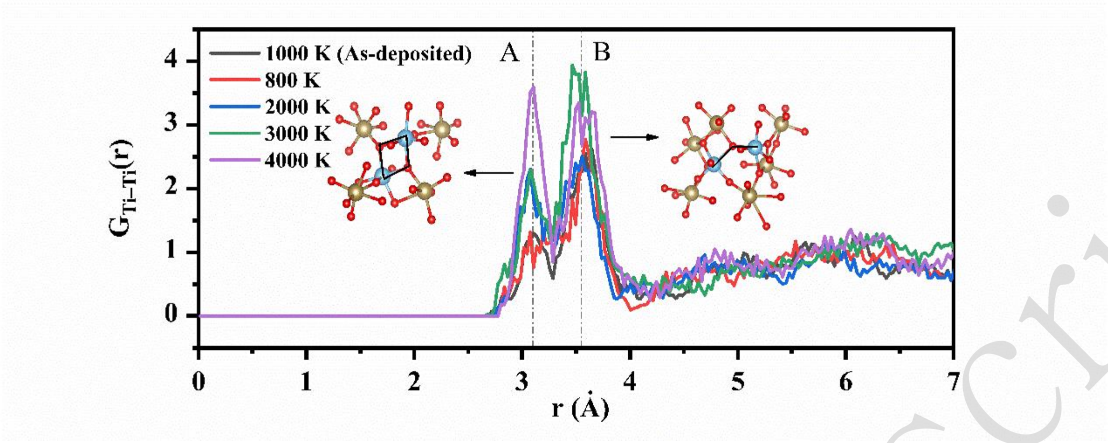

Fig. 11 Normalized Ti–Ti RDFs, $G_{Ti-Ti}(r)$, of the large models as a function of interatomic distance r. Peak A is primarily associated with cyclic Ti–O–Ti bonding configurations, whereas Peak B is mainly attributed to more linear Ti–O–Ti linkages.

To elucidate the evolution of Ti–O clusters during annealing, the normalized Ti–Ti RDFs, denoted as $G_{Ti-Ti}(r)$, were analysed for the large models. Compared to the small (8 atoms) and medium (64 atoms) Ti models, the large model contained 288 Ti atoms, providing sufficient Ti–Ti pair statistics to ensure reliable RDF analysis.

As shown in **Fig. 11**, the as-deposited structure (1000 K, black curve) exhibits two characteristic peaks at 3.12 (Peak A) and 3.57 Å (Peak B). Peak A was primarily associated with cyclic Ti–O–Ti bonding configurations, whereas Peak B was mainly attributed to more linear Ti–O–Ti linkages. These distinct peak positions reflect the different Ti–O–Ti connectivity types within the amorphous network. At 800 K (red curve), the intensities of Peak A and B remain nearly unchanged, whereas a slight increase in the intensity between the two peaks is observed, indicating limited local atomic rearrangements without significant structural reconstruction. At 2000 K (blue curve), the intensity of Peak A increases markedly, suggesting enhanced short-range Ti–Ti correlations and the onset of Ti–O cluster aggregation and structural reorganisation. When the temperature reached 3000 K (green curve), Peak B became significantly more pronounced, reflecting strengthened medium-range Ti–Ti correlations and further cluster growth. At the highest relaxation stage (4000 K, purple curve), Peak B decreased slightly, whereas Peak A increased substantially, indicating a shift of the Ti–Ti correlations toward shorter distances. This behaviour indicates the evolution of relatively extended linear-like configurations toward more compact cyclic-like configurations. Overall, as the degree of structural relaxation increased, the Ti–O clusters progressively aggregated and tended to evolve into more compact cyclic configurations in highly relaxed states.

To further quantify the aggregation behaviour of the Ti atoms, cluster statistics were performed for the medium and large models at different relaxation stages. The number of Ti clusters and Ti atoms within each cluster were analysed. An *n-member cluster* (nMC) was defined as a cluster containing *n* Ti atoms.

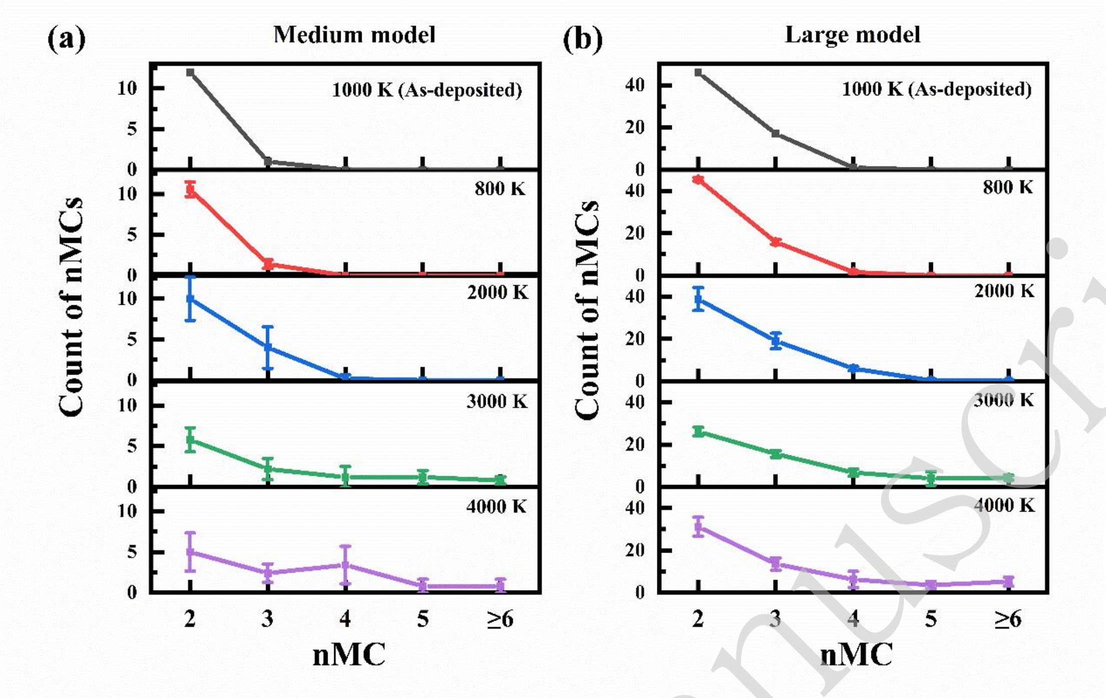

Fig. 12 Statistics on the number of Ti–O clusters and Ti atoms per cluster obtained at different target temperatures for **a** medium and **b** large models. Annealed models were independently generated using five random initial seeds. An *n*-member cluster (nMC) was defined as a cluster containing *n* Ti atoms.

Fig. 12 shows the cluster statistics for different relaxation levels. In the early relaxation stage (800 K), the total number of clusters remained nearly unchanged compared to the as-deposited structure (1000 K). The system was dominated by 2MCs and accompanied by only a small fraction of 3MCs, indicating that the Ti atoms mainly exhibited localised short-range associations. At 2000 K, 4MCs began to emerge in both the medium and large models, suggesting enhanced Ti–Ti correlations and the onset of cluster growth. At higher relaxation level (3000 and 4000 K), the populations of 2MCs and 3MCs decreased slightly, whereas the number of 4MCs continued to increase. Meanwhile, larger clusters, such as 5MCs and clusters containing more than six Ti atoms, emerged and progressively grew in number. This behaviour indicated that smaller Ti clusters gradually merged and reorganised into larger aggregates during structural relaxation. The observed trend is consistent with the enhanced Ti–Ti correlations in the RDF analysis, further supporting progressive Ti aggregation and a tendency toward local Ti enrichment or phase-separation-like behaviour in highly relaxed states.

During annealing, a subset of small models exhibited a clear tendency toward structural ordering. As small models are more sensitive to local structural rearrangements, representative configurations were selected to provide an effective description of the micro-regional structural evolution. **Fig. 13** illustrates the structural changes in these models at different relaxation stages. At relatively low relaxation levels (**Fig. 13a–c**), the system maintained a largely disordered network structure. The 800 K configuration preserved most of the residual structural characteristics inherited from the as-deposited (1000 K) state. Upon relaxation to 2000 K, these residual features were largely eliminated, and the structure remained predominantly amorphous. When the relaxation level was increased to 3000 K, as shown in **Fig. 13d,** a discernible tendency toward ordering emerged along a specific direction. Regular layered features are observable within the black dashed box, indicating the onset of localised structural ordering. At 4000 K (**Fig. 13e**), the layered arrangement became more evident, and periodic features began to develop within the individual layers (highlighted by the green dashed circle). These characteristics exhibit similarities to λ-like orthorhombic structural motifs, although the overall structure remains partially disordered[59].

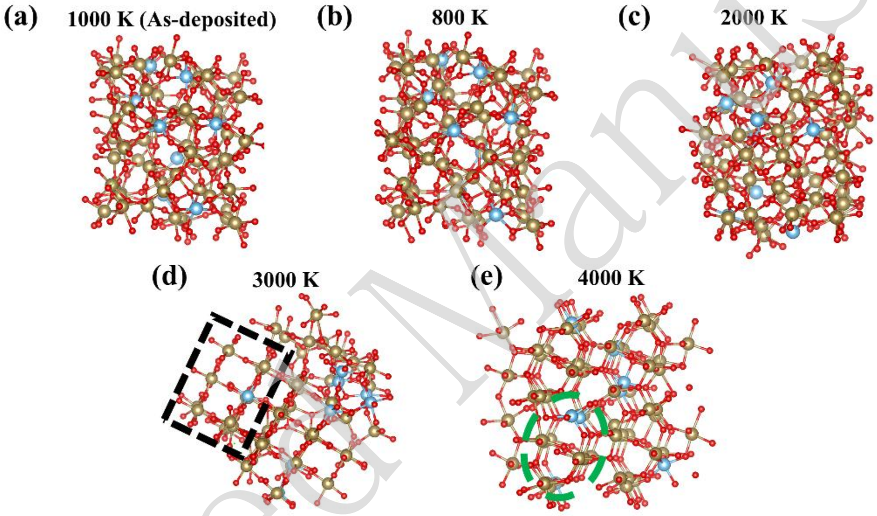

Fig. 13 Atomic structures of small models at different target temperatures (gold, red, and blue represent Ta, O, and Ti atoms, respectively): **a** 1000 (as-deposited), **b** 800, **c** 2000, **d** 3000, and **e** 4000 K. The area marked by the black dashed box in (d) exhibits regular layered characteristics; the area marked by the purple dashed circle in (e) reveals regular periodic characteristics in the intra-layer structure.

To further quantify these structural changes, the RDFs of Ta–O, Ti–O, Ta–Ta, and O–O were calculated for small-sized models (**Fig. 14**). At low relaxation levels (**Fig. 14a–c**), the RDF curves retain typical amorphous features, which is consistent with the structural observations. For the 3000 K configuration (**Fig. 14d**), additional features appeared in the range of 4–8 Å (black dashed circle), corresponding to enhanced second-shell correlations. This indicates an increase in the medium-range structural ordering. At the highest relaxation stage (4000 K; **Fig. 14e**), the intensities of the RDF peaks increased to varying extents, suggesting further enhancement of the structural ordering. Moreover, near the first coordination distances of Ta–O (2.13 Å) and Ti–O (2.02 Å), the originally smooth RDF profiles begin to show slight inflection (red dashed circle). The emergence of such features suggests a redistribution of the bond-length populations, implying a tendency toward more well-defined local bond distances. This effect was more evident for Ta–O, whereas the Ti–O curve exhibited only a subtle inflection. This behaviour implies that the Ta–O and Ti–O polyhedral units undergo structural reorganisation to different extents during relaxation. Notably, the Ti–O first-shell peak becomes somewhat sharper than that of Ta–O, indicating a relatively more uniform local environment around the Ti atoms, which is consistent with the observations reported by Damart et al.[24]. These structural and RDF results suggest that, with increasing relaxation, localised ordering progressively develops within the amorphous TiO_2-Ta_2O_5 system, and a crystallisation tendency may emerge under highly relaxed conditions. This trend is consistent with the morphological evolution observed in the AFM measurements and implies a possible tendency toward local phase separation at advanced relaxation stages.

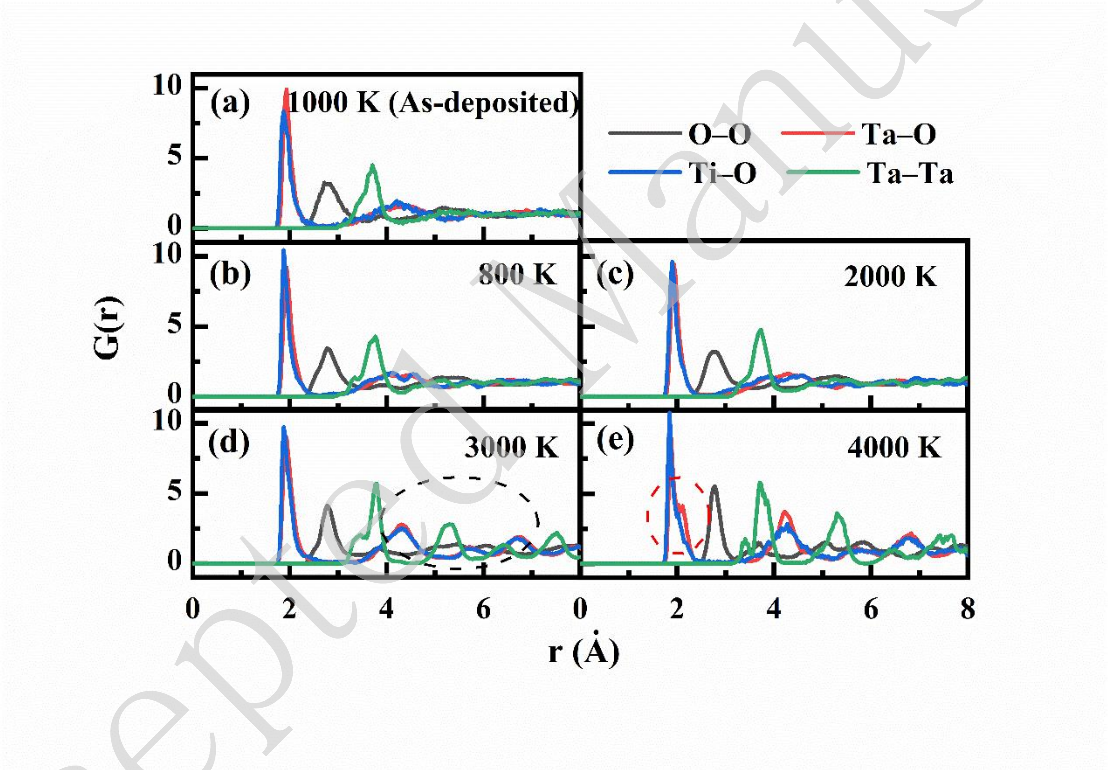

Fig. 14 RDFs of the small-sized models for O–O, Ta–O, Ti–O, and Ta–Ta pairs at different target temperatures: **a** 1000 (as-deposited); **b** 800; **c** 2000; **d** 3000, and **e** 4000 K. The area marked by the black dashed circle in (d) indicate the emergence of second coordination shell features; the area marked by the red dashed circle in (e) indicate slight inflection in the Ta–O and Ti–O RDFs at 2.13 and 2.02 Å, respectively, departing from their previously smooth profiles.

Electronic Structure Modulation: First-Principles Analysis

To investigate the impact of the structural changes on the optical properties of TiO_2-Ta_2O_5, the electronic structure and optical absorption of small models were studied using DFT. For the samples in the as-deposited state and those annealed at lower temperatures, no additional calculations were performed. This is because their atomic position changes are minimal, and previous studies using similar models have confirmed that the induced absorption is primarily attributed to oxygen vacancies, which are strongly composition-dependent rather than structure[15,17,60].

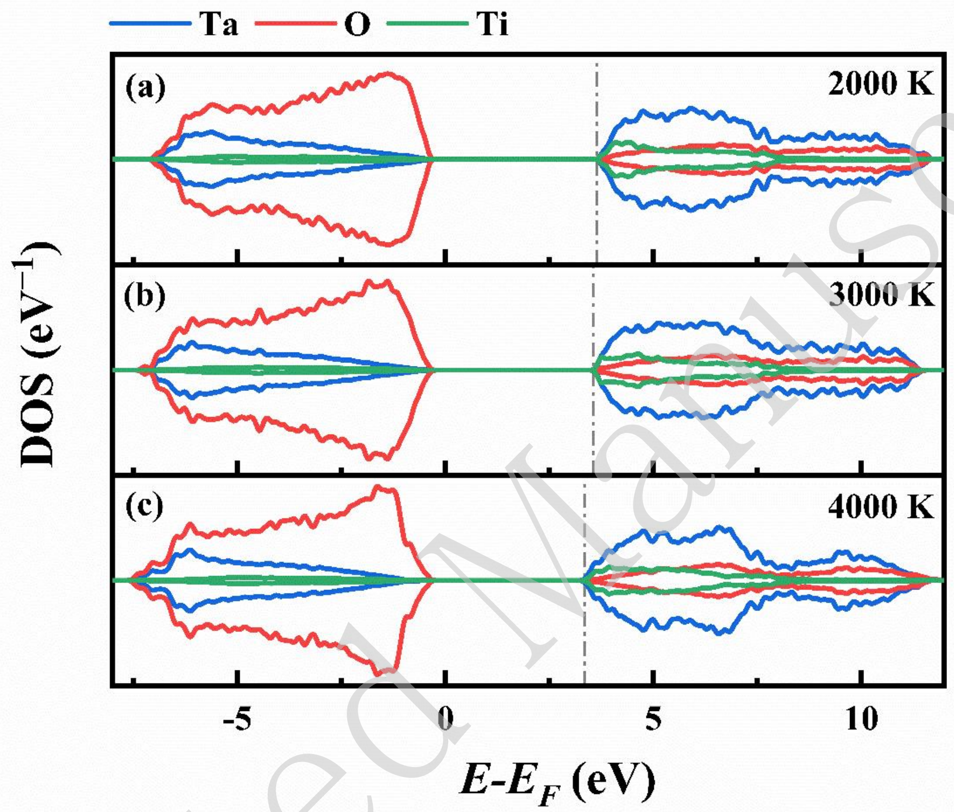

Fig. 15 Density of states (DOS) calculated using the HSE06 hybrid functional for the small models for annealed temperatures of **a** 2000, **b** 3000, and **c** 4000 K. The total magnetic moment of the system was negligible, indicating that the TiO_2-Ta_2O_5 structure remains nonmagnetic.

For the samples annealed at higher temperatures, the electronic structures were calculated at 2000, 3000, and 4000 K to obtain the density of states (DOS) for each element, and the results are shown in **Fig. 15**. Although spin-polarised calculations were performed to account for the possible defect-induced localised states, the total magnetic moment of the system was negligible, indicating that the Ti-doped Ta_2O_5 structure remained nonmagnetic. The apparent mirroring of the DOS along the x-axis arises from the standard spin-resolved representation (spin-up positive and spin-down negative) and does not indicate spin splitting.

Strong hybridisation among the O 2p, Ta 5d, and Ti 3d orbitals was observed in both the valence and conduction bands. The valence band maximum (VBM) was predominantly contributed by the O 2p states, whereas the conduction band minimum (CBM) was mainly derived from the Ta 5d states. As the model closest to the crystalline structure, the 4000 K system (**Fig. 15c**) exhibited more pronounced energy splitting than the 2000 and 3000 K systems. Particularly within the 4–11 eV range, the Ta 5d orbitals tended to split into t_{2g} ($3d_{xy}$, $3d_{xz}$, and $3d_{yz}$) and e_g ($3d_{x^2-y^2}$ and $3d_{z^2}$) orbitals[61]. This indicated a tendency toward structural ordering. Concurrently, the band width progressively narrows with increasing simulated temperature, decreasing from 3.89 eV (2000 K) to 3.76 eV (3000 K), and ultimately to 3.55 eV (4000 K), as indicated by the grey dashed lines in **Fig. 15**. Combined with the structural evolution patterns observed in the MD simulations, this narrowing of the bandwidth is likely attributable to structural anisotropy.

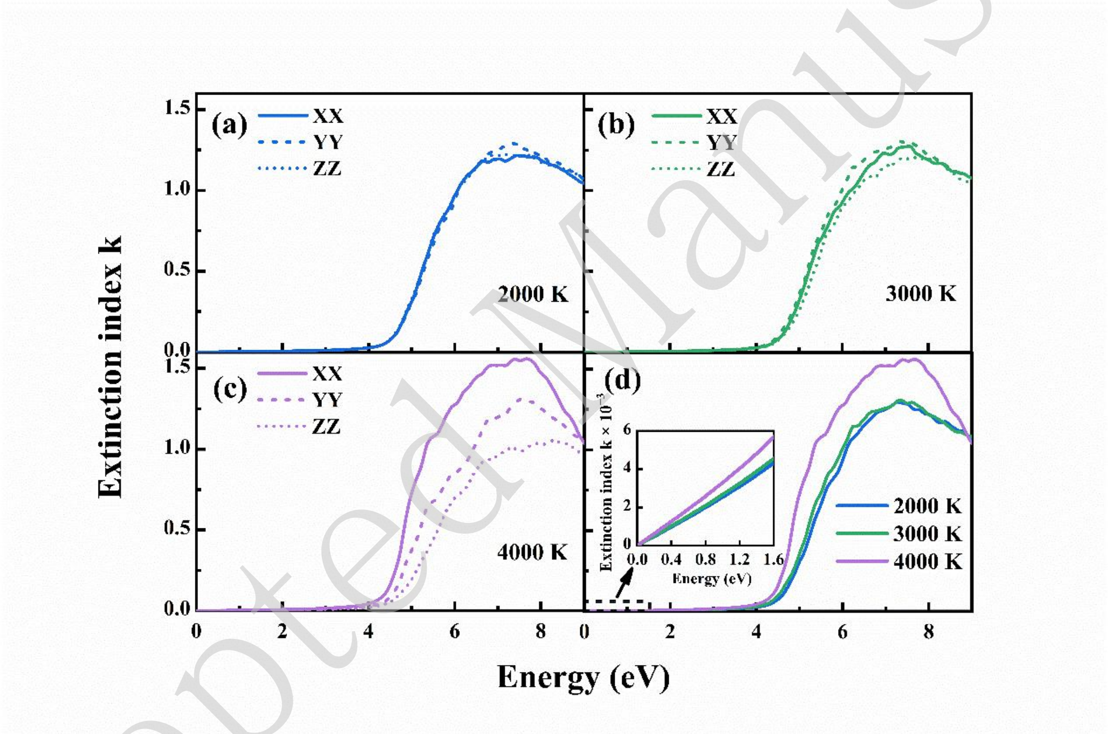

Fig. 16 Extinction coefficient k of the small models calculated using HSE06 hybrid functional. k components in three directions for **a** 2000, **b** 3000, and **c** 4000 K models. **d** Comparison of k for these three models. For the same model, the curve with the highest k within the 0–4 eV range among its three directional components is selected as representative.

This conclusion was further confirmed by calculating the optical properties. **Fig. 16** shows the extinction coefficient (k) curves for the three models, with each plot showing the three directional components: XX, YY, and ZZ. In **Fig. 16a**, the curves for the system annealed at 2000 K nearly overlap across all three directions within 0–6 eV, indicating that the amorphous structure is isotropic. In **Fig. 16b**, the three curves begin to diverge at approximately 4 eV, indicating increased anisotropy in the system. This phenomenon becomes even more pronounced (**Fig. 16c**), as the k curve in the XX direction shifts to the left and deflects upward. This shift may explain the increased absorption observed in films at higher temperatures. For the same model, the curve with the highest k within the 0–4 eV range among its three directional components was selected as representative and is displayed in **Fig. 16d**. The samples annealed at higher temperatures exhibited relatively higher k. The DFT results indicated that with increasing structural ordering, the electronic structure progressively evolved toward TiO_2-like characteristics, accompanied by enhanced anisotropy in the optical response. This trend suggests that structural ordering and local phase enrichment may modify the electronic transitions that contribute to absorption.

It is important to note that the experimentally measured optical absorption in multilayer coatings arises from multiple coupled factors, including structural ordering, defect states, compositional fluctuations, interface scattering, and microstructural inhomogeneities. The purpose of the first-principles calculations in this work was not to reproduce the absolute absorption magnitude, but to isolate and examine the intrinsic influence of structural ordering on the electronic structure and optical response of the TiO_2-Ta_2O_5 system.

Conclusion

In this study, 1064 nm TiO_2-Ta_2O_5 HR coatings prepared by the EB-IAD method were annealed at different temperatures (473–873 K). Annealing in air affected the absorption of TiO_2-Ta_2O_5 films via compositional and structural factors. At lower temperatures, composition contributes more significantly to absorption; when annealing temperatures are 673 K or below, oxygen vacancy defects are the primary cause of film absorption. At higher temperatures, the structural effects dominate. Above 673 K annealing temperatures, film absorption increases sharply, likely due to small-scale crystallisation and phase separation within the amorphous TiO_2-Ta_2O_5. MD simulations coupled with DFT validate this hypothesis. The simulations revealed that increasing the temperature promoted the ordering and aggregation of Ti–O clusters within the amorphous matrix, leading to bandgap narrowing and enhanced structural anisotropy, both of which contributed to increased optical absorption. This work investigated the absorption mechanism of composite laser films, linking the film composition, structural changes, and optical absorption properties. Combined with thermal treatment, the relatively low-cost and highly efficient EB-IAD method enabled the fabrication of TiO_2-Ta_2O_5-based HR mirrors with absorption as low as 1.3 ppm, approaching the level of performance by IBS. This has significant implications for the large-scale mass production of ultralow-absorption optical devices.

Acknowledgements

This work was supported by the Zibo Key Research and Development Project (Grant No. 2020XCCG0106) and the Zibo Key Research and Development Project (Grant

No. 2021SNPT0004).

Author contributions

R. S. performed sample measurements and analysed the data; Z.X. and X.X. conceived and supervised the project, secured funding, and revised the manuscript. K.Z., Y.J., Y.X., and Y.W. prepared the data and polished the manuscript. All the authors contributed to the discussion of the results and approved the final version of the manuscript. R.S., Z.X., and X.X. drafted the manuscript with input from all the authors.

Data Availability Statement

Data supporting the findings of this study are available from the corresponding author upon request.

Conflict of Interest

The authors declare no competing financial interest.

References

1. Zuo, J. X. & Lin, X. C. High‐power laser systems. *Laser & Photonics Reviews* **16**, 2100741 (2022).
2. Schimmel, G. et al. Free space laser telecommunication through fog. *Optica* **5**, 1338 (2018).
3. Gribkov, V. A. et al. Testing of materials perspective for nuclear fusion reactors with inertial plasma confinement by Plasma Focus and laser devices. *Journal of Physics: Conference Series* **1347**, 012071 (2019).
4. Jiao, H. F. et al. $Hf_{1-x}Si_xO_2$ Nanocomposite coatings prepared by ion-assisted co-evaporation process for low-loss and high-LIDT optics. *Materials* **14**, 2606 (2021).
5. Wen, J. H. et al. Research progress on absorption loss control of laser coating. *Acta Optica Sinica* **42**, 0700001 (2022).
6. Liu, W. J., Guo, X. J. & Chien, C. H. The study of optical and microstructural evolution

of Ta_2O_5 and SiO_2 thin films by plasma ion assisted deposition method. *Surface and Coatings Technology* **196**, 69-75 (2005).

7. Chen, C. et al. Effect of ionic oxygen concentration on properties of SiO_2 and Ta_2O_5 monolayers deposited by ion beam sputtering. *Optical Materials* **136**, 113349 (2023).
8. Flaminio, R. et al. A study of coating mechanical and optical losses in view of reducing mirror thermal noise in gravitational wave detectors. *Classical and Quantum Gravity* **27**, 084030 (2010).
9. Abernathy, M. et al. Exploration of co-sputtered Ta_2O_5-ZrO_2 thin films for gravitational-wave detectors. *Classical and Quantum Gravity* **38**, 195021 (2021).
10. Pinard, L. et al. Toward a new generation of low-loss mirrors for the advanced gravitational waves interferometers. *Optics Letters* **36**, 1407 (2011).
11. Harry, G. M. et al. Titania-doped tantala/silica coatings for gravitational-wave detection. *Classical and Quantum Gravity* **24**, 405-415 (2007).
12. Amato, A. et al. Optical and mechanical properties of ion-beam-sputtered Nb_2O_5 and TiO_2-Nb_2O_5 thin films for gravitational-wave interferometers and an improved measurement of coating thermal noise in advanced LIGO. *Physical Review D* **103**, 072001 (2021).
13. Sakiew, W. et al. Influence of ion beam parameters onto two-dimensional optical thin film thickness distributions deposited by ion beam sputtering. *Thin Solid Films* **682**, 109-120 (2019).
14. Farhan, M. S., Zalnezhad, E. & Bushroa, A. R. Properties of Ta_2O_5 thin films prepared by ion-assisted deposition. *Materials Research Bulletin* **48**, 4206-4209 (2013).

15. Chung, T. H. et al. Ultrahigh-reflective optical thin films prepared by reactive magnetron sputtering with RF-induced substrate bias. *Review of Scientific Instruments* **95**, 045107 (2024).
16. Ashraf, L. et al. Structural, electronic, thermoelectric, and optical investigations on Cr substituted Ta_2O_5. *Optical Materials* **148**, 114901 (2024).
17. Song, R. C. et al. Fabrication of ultra-low-absorption thin films via ion beam-assisted electron-beam evaporation. *High Power Laser Science and Engineering* **13**, e38 (2025).
18. Tao, C. X. et al. Imaging photothermal microscopy for absorption measurements of optical coatings. *Chinese Optics Letters* **7**, 1061-1064 (2009).
19. Simpson, R. et al. XPS investigation of monatomic and cluster argon ion sputtering of tantalum pentoxide. *Applied Surface Science* **405**, 79-87 (2017).
20. Plimpton, S. Fast parallel algorithms for short-range molecular dynamics. *Journal of Computational Physics* **117**, 1-19 (1995).
21. Trinastic, J. P. et al. Unified interatomic potential and energy barrier distributions for amorphous oxides. *The Journal of Chemical Physics* **139**, 154506 (2013).
22. Lima, H. et al. Molecular dynamics simulation and crystal field calculations of the Eu_2O_3-PbO-SiO_2 glassy system submitted to long annealing time. *Journal of Non-Crystalline Solids* **448**, 62-67 (2016).
23. Shen, W. Q. et al. Effect of annealing on structural changes and oxygen diffusion in amorphous HfO_2 using classical molecular dynamics. *Journal of Applied Physics* **123**, 085113 (2018).

24. Damart, T. et al. Numerical study of the structural and vibrational properties of amorphous Ta_2O_5 and TiO_2-doped Ta_2O_5. *Journal of Applied Physics* **119**, 175106 (2016).

25. Durandurdu, M. Amorphous zirconia: ab initio molecular dynamics simulations. *Philosophical Magazine* **97**, 1334-1345 (2017).

26. Kresse, G. & Furthmüller, J. Efficiency of ab-initio total energy calculations for metals and semiconductors using a plane-wave basis set. *Computational Materials Science* **6**, 15-50 (1996).

27. Perdew, J. P., Burke, K. & Ernzerhof, M. Generalized gradient approximation made simple. *Physical Review Letters* **77**, 3865-3868 (1996).

28. Heyd, J., Scuseria, G. E. & Ernzerhof, M. Hybrid functionals based on a screened coulomb potential. *The Journal of Chemical Physics* **118**, 8207-8215 (2003).

29. Wang, V. et al. VASPKIT: A user-friendly interface facilitating high-throughput computing and analysis using VASP code. *Computer Physics Communications* **267**, 108033 (2021).

30. Abdellatif, S. et al. Refractive index and scattering of porous TiO_2 films. *Microporous and Mesoporous Materials* **264**, 84-91 (2018).

31. He, X. et al. $CsxWO_3$ films with excellent infrared shielding ability and high visible light transmittance prepared via magnetron sputtering. *Ceramics International* **50**, 45665-45674 (2024).

32. Liu, H. S. et al. Characteristics of optical band gap of tantalum oxide thin film deposited by ion beam sputtering. *Optics and Precision Engineering* **25**, 21-27 (2017).

33. Lv, Q. P. et al. Effects of annealing on residual stress in Ta_2O_5 films deposited by dual ion beam sputtering. *Coatings* **8**, 150 (2018).

34. Lin, Z. S. et al. Effect of annealing on the properties of plasma-enhanced atomic layer deposition grown HfO_2 coatings for ultraviolet laser applications. *Journal of Alloys and Compounds* **946**, 169443 (2023).

35. Niu, X. S. et al. HfO_2/SiO_2 nanolaminate-based composites prepared by ion beam sputtering for low-loss optics. *Optical Engineering* **61**, 031202 (2021).

36. Wen, J. H. et al. Optical and femtosecond laser-induced damage-related properties of Ta_2O_5-based oxide mixtures. *Journal of Alloys and Compounds* **957**, 170352 (2023).

37. Yu, T. et al. The structure and electrical properties of HfTaON high-k films prepared by DIBSD. *Applied Surface Science* **258**, 2953-2958 (2012).

38. Chen, X. B. et al. X-ray spectroscopic study of the electronic structure of visible-light responsive N-, C- and S-doped TiO_2. *Journal of Electron Spectroscopy and Related Phenomena* **162**, 67-73 (2008).

39. Qi, T. G. et al. A micro-structural distortion mechanism on the thermal degradation of $Y_3Al_5O_{12}$: Ce^{3+} phosphor. *Journal of Alloys and Compounds* **731**, 1089-1094 (2018).

40. Bagus, P. S., Nelin, C. J. & Brundle, C. R. Chemical significance of x-ray photoelectron spectroscopy binding energy shifts: a perspective. *Journal of Vacuum Science & Technology A* **41**, 068501 (2023).

41. Dangwal, S. et al. Interfacial engineering of Z-scheme-based 2D/1D -WS_2/TiO_2 heterostructures: enhanced hydrogen evolution reaction and fabrication of facile photoelectrochemical device. *ACS Applied Energy Materials* **8**, 5911-5924 (2025).

42. Rahimi, E. et al. Improved surface charge and corrosion resistance at the near-nanocrystalline chromium/Nano-bilayer oxide interface in advanced thin dense chromium coatings. *Applied Surface Science* **689**, 162504 (2025).

43. Abromavičius, G., Kičas, S. & Buzelis, R. High temperature annealing effects on spectral, microstructural and laser damage resistance properties of sputtered HfO_2 and HfO_2-SiO_2 mixture-based UV mirrors. *Optical Materials* **95**, 109245 (2019).

44. Saputra, R. E., Astuti, Y. & Darmawan, A. Hydrophobicity of silica thin films: the deconvolution and interpretation by Fourier-transform infrared spectroscopy. *Spectrochimica Acta Part A: Molecular and Biomolecular Spectroscopy* **199**, 12-20 (2018).

45. Shchedrina, N. et al. Nano-FTIR spectroscopy reveals SiO_2 densification within fs-laser induced nanogratings. *Nanoscale Advances* **6**, 5164-5170 (2024).

46. Chen, C. et al. Preparation, characterization and visible-light activity of carbon modified TiO_2 with two kinds of carbonaceous species. *Journal of Molecular Catalysis A: Chemical* **314**, 35-41 (2009).

47. Bezrodna, T. et al. Pyridine-TiO_2 surface interaction as a probe for surface active centers analysis. *Applied Surface Science* **214**, 222-231 (2003).

48. Bergler, M. et al. Cooling rate calibration and mapping of ultra-short pulsed laser modifications in fused silica by Raman and Brillouin spectroscopy. *International Journal of Extreme Manufacturing* **2**, 035001 (2020).

49. Joseph, C., Bourson, P. & Fontana, M. D. Amorphous to crystalline transformation in Ta_2O_5 studied by Raman spectroscopy. *Journal of Raman Spectroscopy* **43**,

1146-1150 (2012).

50. Tsuchiya, T. et al. X-Ray absorption, photoemission spectroscopy, and Raman scattering analysis of amorphous tantalum oxide with a large extent of oxygen nonstoichiometry. *Physical Chemistry Chemical Physics* **13**, 17013 (2011).

51. Yang, X. X. et al. Composition- and temperature-resolved Raman shift of silicon. *Applied Spectroscopy* **72**, 598-603 (2018).

52. Meng, J. F. et al. Raman investigation on $(Ta_2O_5)_{1-x}(TiO_2)_x$ system at different temperatures and pressures. *Journal of Physics and Chemistry of Solids* **58**, 1503-1506 (1997).

53. Dobal, P. S. et al. Micro-Raman scattering and x-ray diffraction studies of $(Ta_2O_5)_{1-x}(TiO_2)_x$ ceramics. *Journal of Applied Physics* **87**, 8688-8694 (2000).

54. Kudryavtsev, O. S. et al. Fluorescence and Raman spectroscopy of doped nanodiamonds. *Journal of Applied Spectroscopy* **85**, 295-299 (2018).

55. Pan, Z., Savard, T. & Wicksted, J. P. Raman studies of crystalline and amorphous poly(*p* -phenylene sulfide) films. *Journal of Raman Spectroscopy* **23**, 615-619 (1992).

56. Meletov, K. P. & Efimchenko, V. S. Raman study of hydrogen-saturated silica glass. *International Journal of Hydrogen Energy* **46**, 24501-24509 (2021).

57. Bassiri, R. et al. Probing the atomic structure of amorphous Ta_2O_5 coatings. *Applied Physics Letters* **98**, 031904 (2011).

58. Chen, X. et al. Molecular dynamics study of the effect of titanium ion energy on surface structure during the amorphous TiO_2 films deposition. *Applied Surface Science* **345**, 162-168 (2015).

59. Lee, S. H. et al. Hidden structural order in orthorhombic Ta_2O_5. *Physical Review Letters* **110**, 235502 (2013).

60. Guo, Y. Z. & Robertson, J. Comparison of oxygen vacancy defects in crystalline and amorphous Ta_2O_5. *Microelectronic Engineering* **147**, 254-259 (2015).

61. Zhou, Z. H., Li, M. T. & Guo, L. J. A first-principles theoretical simulation on the electronic structures and optical absorption properties for O vacancy and Ni impurity in TiO_2 photocatalysts. *Journal of Physics and Chemistry of Solids* **71**, 1707-1712 (2010).